

Structural and functional features of central nervous system lymphatic vessels

Antoine Louveau^{1,2}, Igor Smirnov^{1,2}, Timothy J. Keyes^{1,2}, Jacob D. Eccles^{3,4,5}, Sherin J. Rouhani^{3,4,6}, J. David Peske^{3,4,6}, Noel C. Derecki^{1,2}, David Castle⁷, James W. Mandell⁸, Kevin S. Lee^{1,2,9}, Tajie H. Harris^{1,2} & Jonathan Kipnis^{1,2,3}

One of the characteristics of the central nervous system is the lack of a classical lymphatic drainage system. Although it is now accepted that the central nervous system undergoes constant immune surveillance that takes place within the meningeal compartment^{1–3}, the mechanisms governing the entrance and exit of immune cells from the central nervous system remain poorly understood^{4–6}. In searching for T-cell gateways into and out of the meninges, we discovered functional lymphatic vessels lining the dural sinuses. These structures express all of the molecular hallmarks of lymphatic endothelial cells, are able to carry both fluid and immune cells from the cerebrospinal fluid, and are connected to the deep cervical lymph nodes. The unique location of these vessels may have impeded their discovery to date, thereby contributing to the long-held concept of the absence of lymphatic vasculature in the central nervous system. The discovery of the central nervous system lymphatic system may call for a reassessment of basic assumptions in neuroimmunology and sheds new light on the aetiology of neuroinflammatory and neurodegenerative diseases associated with immune system dysfunction.

Seeking to identify routes responsible for the recirculation of surveying meningeal immune cells, we investigated the meningeal spaces and the immune cells that occupy those spaces. First, a whole-mount preparation of dissected mouse brain meninges was developed (Fig. 1a) and stained by immunohistochemistry for endothelial cells (Extended Data Fig. 1a), T cells (Fig. 1b) and major histocompatibility complex II (MHCII)-expressing cells (Extended Data Fig. 1b). Labelling of these cells revealed a restricted partitioning of immune cells throughout the meningeal compartments, with a high concentration of cells found in close proximity to the dural sinuses (Fig. 1b; Extended Data Fig. 1b–d).

The dural sinuses drain blood from both the internal and the external veins of the brain into the internal jugular veins. The exact localization of the T lymphocytes around the sinuses was examined to rule out the possibility of artefacts caused by incomplete intracardial perfusion. Coronal sections of the dura mater (Fig. 1c, d) were stained for CD3e (T cells) and for CD31 (endothelial cells). Indeed, the vast majority of the T lymphocytes near the sinuses were abluminal (Fig. 1e). To confirm this finding, mice were injected intravenously (i.v.) with DyLight 488 lectin or fluorescent anti-CD45 antibody before euthanasia and the abluminal localization was confirmed (Extended Data Fig. 1e, f) and quantified (Fig. 1f). Unexpectedly, a portion of T cells (and of MHCII-expressing cells) was aligned linearly in CD31-expressing structures along the sinuses (only few cells were evident in meningeal blood vessels of similar diameter), suggesting a unique function for these perisinus vessels (Fig. 1g–i).

In addition to the cardiovascular system, the lymphatic vessels represent a distinct and prominent vascular system in the body^{7,8}.

Prompted by our observations, the perisinus vessels were tested for markers associated with lymphatic endothelial cells (LEC). Whole-mount meninges from adult mice were immunostained for the LEC marker, Lyve-1. Two to three Lyve-1-expressing vessels were identified running parallel to the dural sinuses (Fig. 1j, k). Analysis of coronal sections labelled for Lyve-1 and the endothelial cell marker, CD31, revealed that Lyve-1 vessels are located adjacent to the sinus (Fig. 1l) and exhibit a distinct lumen (Fig. 1m). Intravenous injection of DyLight 488 lectin before euthanasia confirmed that these Lyve-1⁺ vessels do not belong to the cardiovascular system (Extended Data Fig. 1g, Supplementary Video 1).

The lymphatic character of the perisinus vessels was further interrogated by assessing the presence of several classical LEC markers. Expression of the main LEC transcription factor, Prox1, was indeed detectable in the Lyve-1⁺ vessels using immunostaining in wild-type mice (Extended Data Fig. 2a) or in transgenic mice expressing tdTomato (tdT) under the Prox1 promoter (Prox1^{tdT}; Fig. 2a). Similar to peripheral lymphatic vessels, the Lyve-1 vessels were also found to express podoplanin (Fig. 2b, Extended Data Fig. 2b, c) and the vascular endothelial growth factor receptor 3 (VEGFR3) (Fig. 2c, Extended Data Fig. 2d). Injection of VEGFR3-specific recombinant VEGF-c into the cisterna magna resulted in an increase in the diameter of the meningeal lymphatic vessels, when examined 7 days after the injection (Fig. 2d, e, Extended Data Fig. 2e), suggesting a functional role of VEGFR3 on meningeal LECs. Finally, the presence of LECs in the meninges was confirmed by flow cytometry; a CD45⁺CD31⁺podoplanin⁺ population of cells (LECs) was detected in the dura mater, and is similar to that found in the skin and diaphragm (Extended Data Fig. 3). We identified a potentially similar structure in human dura (Lyve-1⁺podoplanin⁺CD68⁺; Extended Data Fig. 4), but further studies will be necessary to fully assess and characterize the location and organization of meningeal lymphatic vessels in the human central nervous system.

Two types of afferent lymphatic vessels exist—initial and collecting. They differ anatomically (that is, the presence or absence of surrounding smooth muscle cells and lymphatic valves), in their expression pattern of adhesion molecules^{7,9,10}, and in their permissiveness to fluid and cell entry⁹. In contrast to the sinuses, the meningeal lymphatic vessels are devoid of smooth muscle cells (Fig. 2f, g). Furthermore, meningeal lymphatic vessels were also positive for the immune-cell chemoattractant protein, CCL21 (refs 11, 12; Extended Data Fig. 5a). Unlike the blood vessels that exhibit a continuous pattern of Claudin-5 and vascular endothelial (VE)-cadherin, the meningeal lymphatic vessels exhibit a punctate expression pattern of these molecules similarly to diaphragm lymphatic vessels⁹ (Extended Data Fig. 5b–f). Also, expression of integrin- α 9, which is characteristic of lymphatic valves¹³, was not found on meningeal lymphatic vessels, but was readily detectable in

¹Center for Brain Immunology and Glia, School of Medicine, University of Virginia, Charlottesville, Virginia 22908, USA. ²Department of Neuroscience, School of Medicine, University of Virginia, Charlottesville, Virginia 22908, USA. ³Medical Scientist Training Program, School of Medicine, University of Virginia, Charlottesville, Virginia 22908, USA. ⁴Beirne B. Carter Center for Immunology Research, School of Medicine, University of Virginia, Charlottesville, Virginia 22908, USA. ⁵Department of Medicine (Division of Allergy), School of Medicine, University of Virginia, Charlottesville, Virginia 22908, USA. ⁶Department of Microbiology, Immunology, and Cancer Biology, School of Medicine, University of Virginia, Charlottesville, Virginia 22908, USA. ⁷Department of Cell Biology, School of Medicine, University of Virginia, Charlottesville, Virginia 22908, USA. ⁸Department of Pathology (Neuropathology), School of Medicine, University of Virginia, Charlottesville, Virginia 22908, USA. ⁹Department of Neurosurgery, School of Medicine, University of Virginia, Charlottesville, Virginia 22908, USA.

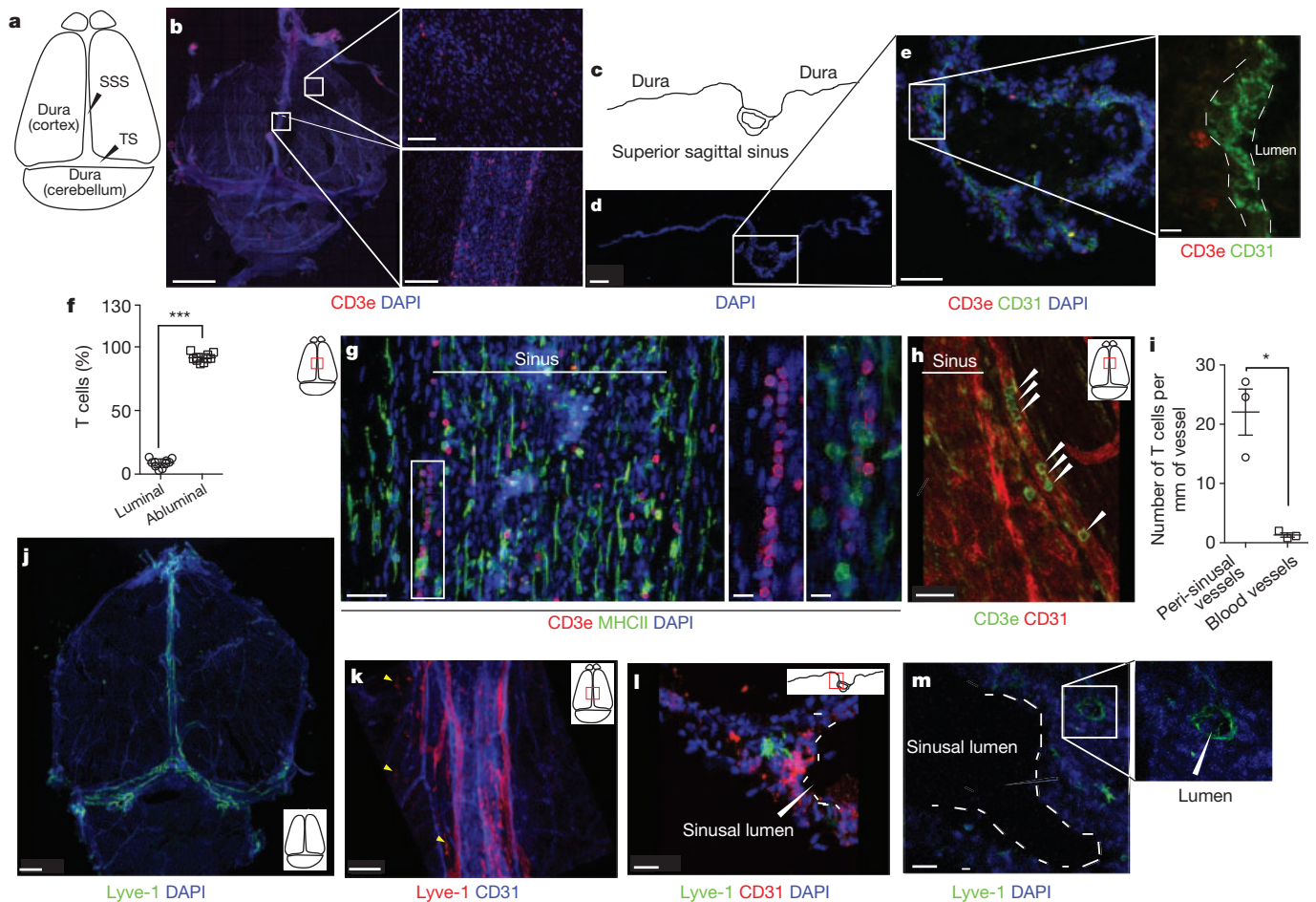


Figure 1 | Abluminal distribution of meningeal T cells and identification of Lyve-1 expressing vessels adjacent to the dural sinuses. **a**, Schematic representation of the whole-mount dissection of the dura mater. SSS, superior sagittal sinus; TS, transverse sinus. **b**, Representative images of CD3e labelling in whole-mount meninges (scale bar, 2,000 μm). Insets, higher magnification of the boxes highlighted in **b** (scale bar, 90 μm (top inset) or 150 μm (bottom inset)). DAPI, 4',6-diamidino-2-phenylindole. **c**, Schematic representation of a coronal section of whole-mount meninges. **d**, Representative image of a coronal section of whole-mount meninges (scale bar, 200 μm). **e**, Representative images of CD3e and CD31 immunolabelling in a coronal section of whole-mount meninges. Scale bar, 100 μm . Inset, higher magnification of the box highlighted in **e** (scale bar, 30 μm , inset, 4 μm). **f**, Quantification of the percentage of sinusal T cells localized ablymally vs luminally to the superior sagittal sinus (mean \pm s.e.m.; $n = 18$ fields analysed from 3 independent animals; $***P = 0.0008$, Mann–Whitney test). **g**, Left, representative images of CD3e and MHCII-expressing cells around the superior sagittal sinus (meningeal

cartoons here and elsewhere depict the location of the presented images; scale bar, 50 μm). Middle, higher magnification of the box highlighted on the left (scale bar, 10 μm). Right, high magnification of CD3- and MHCII-expressing cells (scale bar, 10 μm). **h**, Representative image of CD31 and CD3e labelling around the superior sagittal sinus (scale bar, 30 μm). **i**, Quantification of the number of T cells per mm of vessels in the perisinusal CD31⁺ vessels and in similar diameter meningeal blood vessels (mean \pm s.e.m.; $n = 3$ animals; $*P = 0.05$, one-tailed Mann–Whitney test). **j**, Representative image of Lyve-1 labelling on whole-mount meninges (scale bar, 1,000 μm). **k**, Higher magnification of Lyve-1-expressing vessels (scale bar, 70 μm); arrowheads indicate Lyve-1⁺ macrophages. **l**, Representative images of CD31 and Lyve-1 labelling of a coronal section of the superior sagittal sinus (scale bar, 70 μm). **m**, Higher magnification of a Lyve-1-positive vessel presenting a conduit-like structure (scale bar, 50 μm). Inset, $\times 1.7$ magnification of the Lyve-1⁺ vessel presented in **m**; arrowhead points to the lumen of the vessel.

the skin lymphatic network (Extended Data Fig. 5g, h). Collectively, these findings indicate that the meningeal lymphatic vessels possess anatomical and molecular features characteristic of initial lymphatic vessels. Furthermore, electron microscopy of whole-mount meninges revealed typical ultrastructural characteristics¹⁴ of the lymphatic vessels, which exhibited a non-continuous basement membrane surrounded by anchoring filaments (Fig. 2h, Extended Data Fig. 5i).

While possessing many of the same attributes as peripheral lymphatic vessels, the general organization and distribution of the meningeal lymphatic vasculature displays certain unique features. The meningeal lymphatic network appears to start from both eyes and track above the olfactory bulb before aligning adjacent to the sinuses (Supplementary Video 2). Compared to the diaphragm, the meningeal lymphatic network covers less of the tissue and forms a less complex network composed of narrower vessels (Extended Data Fig. 5j; Supplementary

Video 2). The vessels are larger and more complex in the transverse sinuses than in the superior sagittal sinus (Extended Data Fig. 5j). The differences in the vessel network could be due to the environment in which the vessels reside—the high cerebrospinal fluid pressure in the central nervous system compared to the interstitial fluid pressure in peripheral tissues could affect the branching of the vessels and also limit their expansion.

Next, the functional capability of the meningeal lymphatic vessels to carry fluid and cells from the meninges/cerebrospinal fluid was examined. Anaesthetized adult mice were simultaneously injected with fluorescein i.v. and with fluorescent tracer dye (QDot655) intracerebroventricularly (i.c.v.), and then imaged through thinned skull by multiphoton microscopy. Vessels filled with QDot655, but not with fluorescein, were seen aligned along the superior sagittal sinus (Fig. 3a–d; Supplementary Video 3), suggesting that non-cardiovascular vessels drain cerebrospinal fluid. This cerebrospinal fluid drainage into

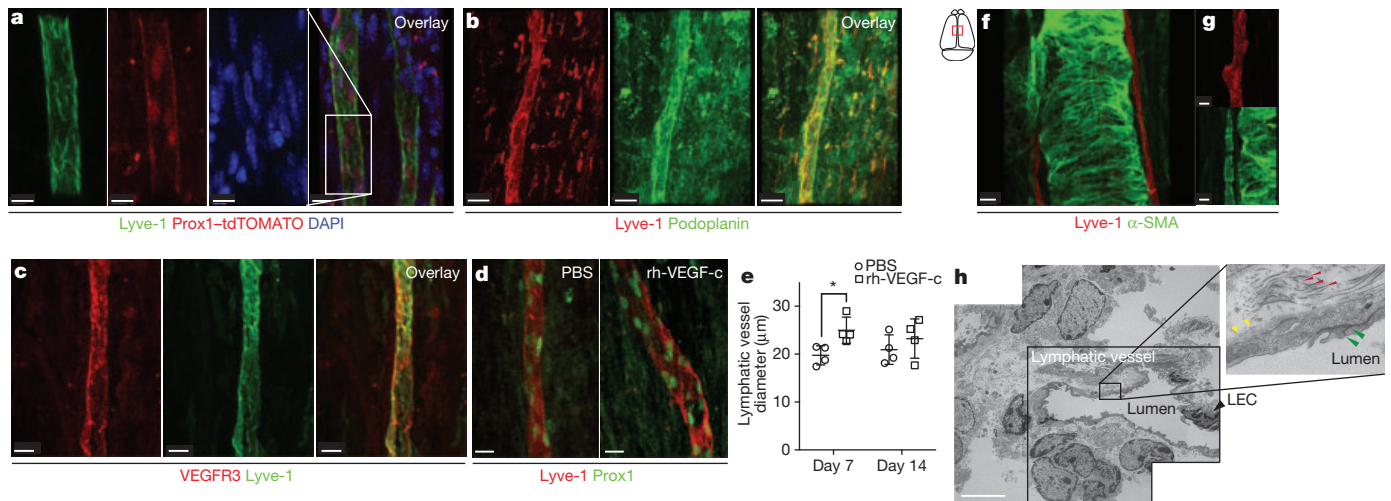


Figure 2 | Molecular and structural characterization of meningeal lymphatic vessels. **a**, Representative images of Prox1 expression in the nuclei of Lyve-1⁺ vessels in the dural sinuses of Prox1^{tdT} mice (scale bars, 10 µm). **b**, Representative images of podoplanin and Lyve-1 labelling on dural sinuses (scale bar, 40 µm). **c**, Representative images of VEGFR3 and Lyve-1 staining on dural sinuses (scale bar, 20 µm). **d**, **e**, Adult mice were injected i.c.v. (cisterna magna) with 4 µg of rhVEGF-c (Cys156Ser) or with PBS. Meninges were harvested 7 and 14 days after the injection. **d**, Representative images of Lyve-1 and Prox1 labelling of meninges at day 7 after injection (scale bars, 30 µm).

e, Quantification of the meningeal lymphatic vessel diameter (mean ± s.e.m.; $n = 4$ mice each group; * $P < 0.05$, two-way ANOVA with Bonferroni post hoc test). **f**, **g**, Representative images of smooth muscle cells (alpha-smooth muscle actin, α -SMA) and Lyve-1 labelling on dural sinuses (scale bars, 50 µm (**g**) or 20 µm (**f**)). **h**, Representative low power micrograph (transmission electron microscopy) of a meningeal lymphatic vessel (scale bar, 5 µm). Inset, higher magnification of the box highlighted in **h**. Yellow arrowheads, basement membrane; red arrowheads, anchoring filaments (collagen fibres); green arrowheads, cellular junction.

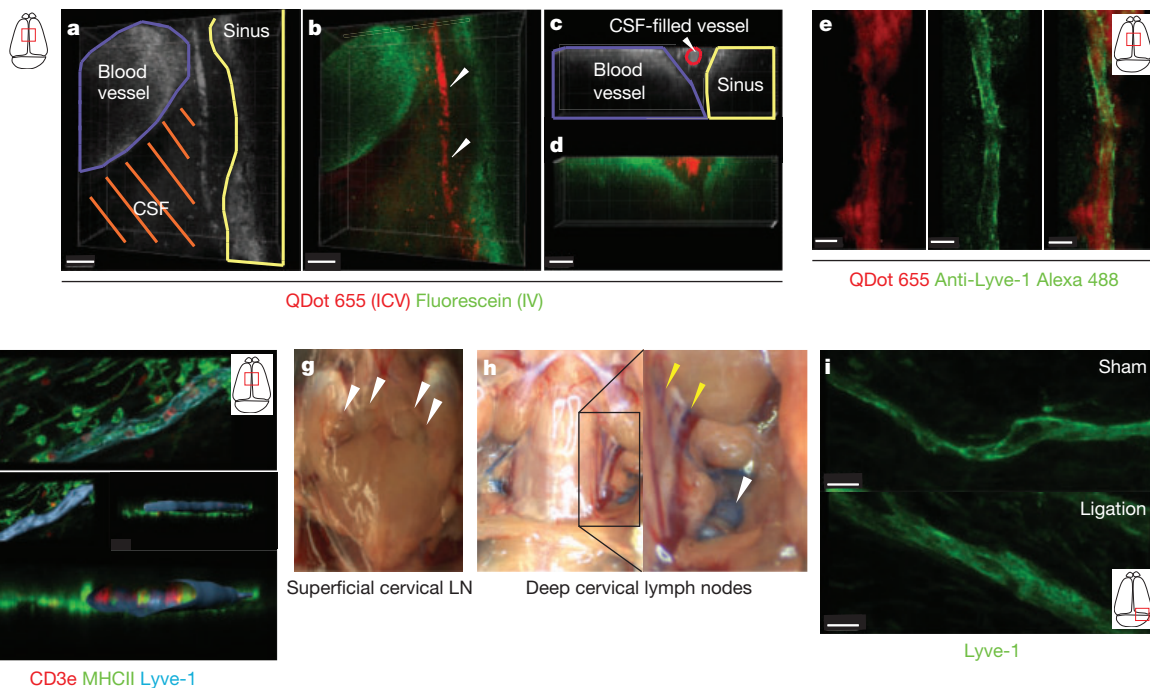


Figure 3 | Functional characterization of meningeal lymphatic vessels. **a-d**, Representative z-stacks of the superior sagittal sinus of adult mice injected intravenously (i.v.) with fluorescein and intracerebroventricularly (i.c.v.) with QDot655 ($n = 3$ mice). **a**, **b**, Low-magnification images showing fluorescein labelling in a meningeal blood vessel and in the superior sagittal sinus (scale bars, 20 µm in **a**, **b**). In contrast, QDot655 labelling is prominent in the perisinusoidal vessel. **c**, **d**, Coronal section of the z-stack presented in **a** and **b** (scale bars, 20 µm in **c**, **d**). CSF, cerebrospinal fluid. **e**, Representative z-stack of cerebrospinal fluid-filled vessel from a mouse injected i.c.v. with both QDot655 and Alexa488-conjugated anti-Lyve-1 antibody ($n = 3$ mice; scale bars, 30 µm). **f**, Top, representative image of immunolabelling for CD3e and MHCII along with Lyve-1 in the meninges (scale bar, 15 µm). Bottom, representative image of a 3D reconstruction of the meningeal lymphatic vessels showing the luminal

localization of the CD3e and MHCII-expressing cells (scale bar, 20 µm). **g**, **h**, Adult mice were injected i.c.v. with 5 µl of 10% Evans blue. Superficial cervical lymph nodes (**g**) and deep cervical lymph nodes (**h**) were analysed 30 min after injection ($n = 5$ mice); white arrowheads indicate the lymph nodes; yellow arrowheads indicate the Evans blue-filled vessels arising near the internal jugular vein into the deep cervical lymph nodes (**h**). **i**, **j**, The collecting vessels draining into the deep cervical lymph nodes (yellow arrowheads in **h**) were ligated or sham-operated. Eight hours after the ligation, the meninges were collected and immunolabelled for Lyve-1. Representative images of immunolabelling for Lyve-1 in the transverse sinus of ligated and sham-operated mice (**i**; scale bars, 30 µm). Dot plots represent measurement of the meningeal lymphatic vessel diameters (**j**; mean ± s.e.m.; $n = 5$ mice each group from 2 independent experiments; * $P = 0.031$, Mann-Whitney test).

meningeal vessels may occur in addition to the previously described cerebrospinal fluid filtration into the dural sinuses via arachnoid granulations^{15,16} (Extended Data Fig. 6a). Injection of Alexa488-conjugated anti-Lyve-1 antibody i.c.v. labelled the meningeal lymphatic vessels (Extended Data Fig. 6b, c; Supplementary Video 4). Moreover, co-injection of a QDot655 and an Alexa488-conjugated anti-Lyve-1 antibody i.c.v. demonstrated that the meningeal lymphatic vessels were indeed filled with QDot655, and thus were draining the cerebrospinal fluid (Fig. 3e). Imaging of the QDot655-filled lymphatic vessels revealed a slower flow rate but similar direction of flow in the meningeal lymphatic vessels compared to the adjacent blood vessels (Supplementary Video 5), similar to what is observed outside of the central nervous system¹⁷.

Classic lymphatic vessels, in addition to draining interstitial fluids, allow cells to travel from tissues to draining lymph nodes¹⁸. We therefore examined whether the meningeal lymphatic vessels were capable of carrying leukocytes. Immunohistochemical analysis of whole-mount meninges revealed that ~24% of all sinusoidal T cells and ~12% of all sinusoidal MHCII⁺ cells were found within these vessels (Fig. 3f, Extended Data Fig. 7a, b). Moreover, CD11c⁺ cells and B220⁺ cells are also found in the meningeal lymphatic vessels of naive mice (Extended Data Fig. 7c–f).

Cellular and soluble constituents of the cerebrospinal fluid have been shown to elicit immune responses in the cervical lymph nodes^{19–22}. Their proposed path is via the cribriform plate into lymphatic vessels within the nasal mucosa²³. To determine whether meningeal lymphatic vessels communicate with deep cervical lymph nodes directly, we injected mice with Evans blue i.c.v. and examined peripheral lymph nodes for the presence of the dye over a 2 h period. Thirty minutes after injection, Evans blue was detected in the meningeal lymphatic vessels and the sinus, as expected (Extended Data Fig. 8a–c), and had also drained into the deep cervical lymph nodes (dCLN) (Fig. 3g, h), but not into the superficial cervical lymph nodes. At later time points, Evans blue was also present in the superficial cervical lymph nodes (data not shown). Virtually no Evans blue was seen in the surrounding non-lymphatic tissue at the time points tested. Interestingly, no Evans blue was detected in the dCLN 30 min after direct injection into the nasal mucosa (Extended Data Fig. 8d, e), suggesting that meningeal lymphatic vessels and not nasal mucosa lymphatic vessels represent the primary route for drainage of cerebrospinal fluid-derived soluble and cellular constituents into the dCLN during this time frame.

Resection of the dCLN affected the T-cell compartment of the meninges, resulting in an increase in the number of meningeal T cells (Extended Data Fig. 9a–e). This presumably resulted from an inability of T cells to drain from the meningeal spaces, consistent with a direct connection between the meninges and the dCLN. To further demonstrate this connection, we ligated the lymph vessels that drain into the dCLNs (Extended Data Fig. 9f), and injected the mice i.c.v. with Evans blue. No accumulation of Evans blue was evident in the dCLN of ligated mice, as opposed to dye accumulation in the sham-operated controls (Extended Data Fig. 9g). Moreover, an increase in the diameter of the meningeal lymphatic vessels was observed (Fig. 3i, j; Extended Data Fig. 9h), similar to lymphoedema observed in peripheral tissues²⁴. These results further suggest physical connection between the meningeal lymphatic vessels and the dCLN.

Drainage of the cerebrospinal fluid into the periphery has been a subject of interest for decades and several routes have been described regarding how cerebrospinal fluid can leave the central nervous system^{23,25}. The newly discovered meningeal lymphatic vessels are a novel path for cerebrospinal fluid drainage and represent a more conventional path for immune cells to egress the central nervous system. Our findings may represent the second step in the drainage of the interstitial fluid from the brain parenchyma into the periphery after it has been drained into the

cerebrospinal fluid through the recently discovered glymphatic system^{26,27} (Extended Data Fig. 10).

The presence of a functional and classical lymphatic system in the central nervous system suggests that current dogmas regarding brain tolerance and the immune privilege of the brain should be revisited. Malfunction of the meningeal lymphatic vessels could be a root cause of a variety of neurological disorders in which altered immunity is a fundamental player such as multiple sclerosis, Alzheimer's disease, and some forms of primary lymphoedema that are associated with neurological disorders^{28–30}.

Online Content Methods, along with any additional Extended Data display items and Source Data, are available in the online version of the paper; references unique to these sections appear only in the online paper.

Received 30 October 2014; accepted 20 March 2015.

Published online 1 June 2015.

- Ransohoff, R. M. & Engelhardt, B. The anatomical and cellular basis of immune surveillance in the central nervous system. *Nature Rev. Immunol.* **12**, 623–635 (2012).
- Kipnis, J., Gadani, S. & Derecki, N. C. Pro-cognitive properties of T cells. *Nature Rev. Immunol.* **12**, 663–669 (2012).
- Shechter, R., London, A. & Schwartz, M. Orchestrated leukocyte recruitment to immune-privileged sites: absolute barriers versus educational gates. *Nature Rev. Immunol.* **13**, 206–218 (2013).
- Goldmann, J. et al. T cells traffic from brain to cervical lymph nodes via the cribriform plate and the nasal mucosa. *J. Leukoc. Biol.* **80**, 797–801 (2006).
- Kaminski, M. et al. Migration of monocytes after intracerebral injection at entorhinal cortex lesion site. *J. Leukoc. Biol.* **92**, 31–39 (2012).
- Engelhardt, B. & Ransohoff, R. M. The ins and outs of T-lymphocyte trafficking to the CNS: anatomical sites and molecular mechanisms. *Trends Immunol.* **26**, 485–495 (2005).
- Alitalo, K. The lymphatic vasculature in disease. *Nature Med.* **17**, 1371–1380 (2011).
- Wang, Y. & Oliver, G. Current views on the function of the lymphatic vasculature in health and disease. *Genes Dev.* **24**, 2115–2126 (2010).
- Baluk, P. et al. Functionally specialized junctions between endothelial cells of lymphatic vessels. *J. Exp. Med.* **204**, 2349–2362 (2007).
- Kerjaschki, D. The lymphatic vasculature revisited. *J. Clin. Invest.* **124**, 874–877 (2014).
- Debes, G. F. et al. Chemokine receptor CCR7 required for T lymphocyte exit from peripheral tissues. *Nature Immunol.* **6**, 889–894 (2005).
- Weber, M. et al. Interstitial dendritic cell guidance by haptotactic chemokine gradients. *Science* **339**, 328–332 (2013).
- Bazigou, E. et al. Integrin- $\alpha 9$ is required for fibronectin matrix assembly during lymphatic valve morphogenesis. *Dev. Cell* **17**, 175–186 (2009).
- Koina, M. E. et al. Evidence for lymphatics in the developing and adult human choroid. *Invest. Ophthalmol. Vis. Sci.* **56**, 1310–1327 (2015).
- Johanson, C. E. et al. Multiplicity of cerebrospinal fluid functions: new challenges in health and disease. *Cerebrospinal Fluid Res.* **5**, 10 (2008).
- Weller, R. O., Djuanda, E., Yow, H.-Y. & Carare, R. O. Lymphatic drainage of the brain and the pathophysiology of neurological disease. *Acta Neuropathol.* **117**, 1–14 (2009).
- Liu, N.-F., Lu, Q., Jiang, Z.-H., Wang, C.-G. & Zhou, J.-G. Anatomic and functional evaluation of the lymphatics and lymph nodes in diagnosis of lymphatic circulation disorders with contrast magnetic resonance lymphangiography. *J. Vasc. Surg.* **49**, 980–987 (2009).
- Girard, J.-P., Moussion, C. & Förster, R. HEVs, lymphatics and homeostatic immune cell trafficking in lymph nodes. *Nature Rev. Immunol.* **12**, 762–773 (2012).
- Weller, R. O., Galea, I., Carare, R. O. & Minagar, A. Pathophysiology of the lymphatic drainage of the central nervous system: implications for pathogenesis and therapy of multiple sclerosis. *Pathophysiology* **17**, 295–306 (2010).
- Mathieu, E., Gupta, N., Macdonald, R. L., Ai, J. & Yücel, Y. H. *In vivo* imaging of lymphatic drainage of cerebrospinal fluid in mouse. *Fluids Barriers CNS* **10**, 35 (2013).
- Cserr, H. F., Harling-Berg, C. J. & Knopf, P. M. Drainage of brain extracellular fluid into blood and deep cervical lymph and its immunological significance. *Brain Pathol.* **2**, 269–276 (1992).
- Harris, M. G. et al. Immune privilege of the CNS is not the consequence of limited antigen sampling. *Sci. Rep.* **4**, 4422 (2014).
- Laman, J. D. & Weller, R. O. Drainage of cells and soluble antigen from the CNS to regional lymph nodes. *J. Neuroimmune Pharmacol.* **8**, 840–856 (2013).
- Schneider, M., Ny, A., Ruiz de Almodovar, C. & Carmeliet, P. A new mouse model to study acquired lymphoedema. *PLoS Med.* **3**, e264 (2006).
- Kida, S., Pantazis, A. & Weller, R. O. CSF drains directly from the subarachnoid space into nasal lymphatics in the rat. Anatomy, histology and immunological significance. *Neuropathol. Appl. Neurobiol.* **19**, 480–488 (1993).
- Xie, L. et al. Sleep drives metabolite clearance from the adult brain. *Science* **342**, 373–377 (2013).
- Yang, L. et al. Evaluating glymphatic pathway function utilizing clinically relevant intrathecal infusion of CSF tracer. *J. Transl. Med.* **11**, 107 (2013).

28. Berton, M. *et al.* Generalized lymphedema associated with neurologic signs (GLANS) syndrome: A new entity? *J. Am. Acad. Dermatol.* **72**, 333–339 (2015).
29. Akiyama, H. *et al.* Inflammation and Alzheimer's disease. *Neurobiol. Aging* **21**, 383–421 (2000).
30. Hohlfeld, R. & Wekerle, H. Immunological update on multiple sclerosis. *Curr. Opin. Neurol.* **14**, 299–304 (2001).

Supplementary Information is available in the online version of the paper.

Acknowledgements We thank S. Smith for editing the manuscript; V. Engelhard for initial discussions and suggestions on lymphatic endothelial cell specific markers. We also thank the members of the Kipnis laboratory, Brain Immunology and Glia (BIG) center, and the Department of Neuroscience at the University of Virginia (especially J. Lukens) for their valuable comments during multiple discussions of this work. L. Holland and B. Lopes provided the human samples. This work was funded by "Fondation pour la Recherche Medicale" to A.L. and by The National Institutes of Health (R01AG034113 and R01NS061973) to J.K.

Author Contributions A.L. performed most of the experiments, analysed the data, and contributed to experimental design and manuscript writing. I.S. performed all the surgeries and intracerebroventricular injections. T.J.K. assisted with the experiments and the analysis of the data. J.D.E, S.J.R. and J.D.P. participated in the discussions and helped with the experimental design. N.C.D. performed the xDCLN experiment. D.C. contributed to the imaging and the analysis of the electron microscopy images. J.W.M. contributed with data analysis of the human samples. K.S.L. contributed to experimental design and to manuscript editing. T.H.H. assisted to the intravital imaging experiment, contributed to experimental design and to manuscript editing. J.K. designed the study, assisted with data analysis, and wrote the manuscript.

Author Information Reprints and permissions information is available at www.nature.com/reprints. The authors declare no competing financial interests. Readers are welcome to comment on the online version of the paper. Correspondence and requests for materials should be addressed to A.L. (al2hk@virginia.edu) or J.K. (kipnis@virginia.edu).

METHODS

No statistical methods were used to predetermine sample size.

Animals. Male and female C57Bl/6, *NOD.Cd11c-YFP* and *Prox1^{tdT}* mice were purchased from Jackson Laboratories and were housed in temperature and humidity controlled rooms, maintained on a 12 h/12 h light/dark cycle (lights on at 7:00). All strains were kept in identical housing conditions. All procedures complied with regulations of the Institutional Animal Care and Use Committee at University of Virginia. Only adult animals (eight to ten weeks) were used in this study. Sample size was chosen in accordance with similar, previously published experiments. Animals from different cages in the same experimental group were selected to assure randomization. For all experiments, investigators were blinded from the time of euthanasia to the end of the analysis.

Human samples. Autopsy specimens of human dura including the superior sagittal sinus were obtained from the Departments of Pathology and Neurosurgery at the University of Virginia. All samples are from consenting patients that gave no restriction to the use of their body for research and teaching (through the Virginia Anatomical Board, Richmond, VA). All obtained samples were fixed and stored in a 10% formalin solution for prolonged time periods.

Meninges immunohistochemistry. Mice were euthanized with an intraperitoneal (i.p.) injection of Euthasol and perfused with 0.1 M of PBS for 5 min. Skin was removed from the head and the muscle was stripped from the bone. After removal of the mandibles and the skull rostral to maxillae, the top of the skull was removed with surgical scissors. Whole-mount meninges were fixed while still attached to the skull cap in PBS with 2% paraformaldehyde (PFA) for 24 h at 4 °C or in 1:1 ethanol:acetone solution for 20 min at -20 °C depending on the antibody. The dura/arachnoid was then dissected from the skullcap. For analysis of the pia mater, brains extracted from the skull were flash frozen, and 40 µm-thick transverse sections were sliced using a cryostat (Leica). The choroid plexus was dissected out of the ventricles of non-fixed brain and fixed with 2% PFA in PBS for 24 h. For coronal sectioning of whole-mount meninges, 100 µl of Matrigel (Corning) was injected into the dural sinuses before dissection. The meninges (dura mater/arachnoid) were dissected from the skullcap, flash frozen, and 10-µm thick sections were cut using a cryostat, and the slices were placed on gelatin-coated slides.

Whole mounts and sections were incubated with PBS containing 2% of normal serum (either goat or chicken), 1% BSA, 0.1% Triton-X-100 and 0.05% of Tween 20 for 1 h at room temperature, followed by incubation with appropriate dilutions of primary antibodies: anti-CD31 (eBioscience, clone 390, 1:100); anti-CD3e (eBioscience, clone 17A2, 1:500), anti-MHC II (eBioscience, clone M5/114.15.2, 1:500), anti-Lyve-1 (eBioscience, clone ALY7, 1:200), anti-Prox1 (Angiobio, 11-002, 1:500), anti-podoplanin (eBioscience, clone 8.1.1, 1:100), anti-VEGFR3 (R&D Systems, AF743, 1:100), anti-α-SMA (Sigma-Aldrich, clone 1A4, 1:500), anti-VE-Cadherin (eBioscience, clone BV13 1:100), anti-Claudin-5 (Molecular Probes, 352588, 1:200), anti-CCL21 (R&D Systems, AF457, 1:100), anti integrin-α9 (R&D Systems, AF3827, 1:100), anti-B220 (eBioscience, clone RA3-6B2, 1:100), anti CD11c (eBioscience, clone N418, 1:100) overnight at 4 °C in PBS containing 1% BSA and 0.5% Triton-X-100. Whole mounts and sections were then washed 3 times for 5 min at room temperature in PBS followed by incubation with Alexafluor 488/594/647 chicken/goat anti rabbit/goat IgG antibodies (Invitrogen, 1:1,000) or PE/Cy3 conjugated streptavidin (eBioscience, 1:1,000) for 1 h at room temperature in PBS with 1% BSA and 0.5% Triton-X-100. After 5 min in 1:10,000 DAPI reagent, whole mount and section were washed with PBS and mounted with Aqua-Mount (Lerner) under coverslips. For the pre-absorption experiments, the anti-VEGFR3 and anti-podoplanin antibodies were incubated respectively with recombinant mouse VEGFR3 (743-R3-100, R&D Systems) or recombinant mouse podoplanin (3244-PL-050, R&D Systems) at the concentration ratio of 1:10 overnight at 4 °C in PBS containing 1% BSA and 0.5% Triton-X-100 before staining.

For human samples, formalin-fixed superior sagittal sinuses were dissected in 2-mm thick sections and fixed overnight in PBS with 4% PFA. Tissues were then embedded in OCT and 10-µm thick sections were sliced onto gelatin-coated slides on a cryostat (Leica). Antigen retrieval was performed by incubation of the slides for 20 min in sodium citrate buffer pH 6.0 at 80 °C. After washing with PBS, endogenous biotins were blocked with a 30 min incubation in PBS with 3% H₂O₂, then the slides were blocked in PBS containing 2% of normal goat serum, 1% BSA, 0.1% Triton-X-100 and 0.05% Tween 20 for 1 h at room temperature. Slides were then incubated overnight at 4 °C with anti-Lyve-1 (ab36993, Abcam, 1:200), anti-podoplanin (HPA007534, Sigma-Aldrich, 1:200) or anti-CD68 (HPA048982, Sigma-Aldrich, 1:1,000) diluted in PBS with 1% BSA and 0.5% Triton-X-100. Sections were then washed 3 times for 5 min at room temperature in PBS followed by incubation with biotin-conjugated goat anti-rabbit antibody (Jackson ImmunoResearch, 1:1,000) for 1 h at room temperature, then for 30 min at room temperature with ABC kit solutions (Vectastain, Vector Labs). Slides were then incubated with the peroxidase substrate DAB (Sigma-Aldrich) for several

minutes, counterstained with haematoxylin, dehydrated, and mounted in Cytoseal 60 (Thermo Scientific) under coverslips. Nine human samples were labelled and analysed; the lymphatic structures were identified in two of them.

Image analysis. Images were acquired with a Leica TCS SP8 confocal system (Leica Microsystems) using the LAS AF Software. For the images of the complete whole mount, images were acquired with a ×10 objective with 0.25 NA. Other confocal images were acquired using a ×20 objective with 0.70 NA or a ×40 oil immersion objective with 1.30 NA. All images were acquired with a 512 × 512 pixel resolution and with a z-step of 4 µm. Quantitative assessments were performed using FIJI software (NIH). Percentage of luminal T cells was determined by counting the number of T cells with luminal localization in the sinuses area. T cell density was established by dividing the number of T lymphocytes by the area of meninges. Prox1-positive cell density was defined by dividing the number of Prox1⁺ nuclei by the area of lymphatic vessels. Statistical analyses were performed using GraphPad Prism software. Specific statistical tests are presented in the text for each experiment. Outlier samples were eliminated using the Grubbs' test with a significance level of 0.01 (only for the rh-VEGF-c experiment). No estimate of variation between groups was performed.

Electron microscopy. Meninges were harvested as previously described and fixed in 2.5% glutaraldehyde, 2% paraformaldehyde in 0.1 M sodium cacodylate buffer, pH 7.4, and post-fixed in 2% osmium tetroxide in 0.1 M cacodylate buffer with 0.15% potassium ferrocyanide. After rinsing in buffer, the tissue was dehydrated through a series of graded ethanol to propylene oxide, infiltrated and embedded in epoxy resin and polymerized at 70 °C overnight. Semi-thin sections (0.5 µm) were stained with toluidine blue for light microscope examination. Ultrathin sections (80 nm) were cut (Integrated microscopy centre, University of Memphis) and imaged using the Tecnai TF20 TEM with an AMT XR41 camera (Extended Data Fig. 5); Integrated microscopy centre, University of Memphis) or using the Tecnai F20 TEM with an UltraScan CCD camera (Fig. 2h; Advanced Microscopy core, University of Virginia).

Multiphoton microscopy. Mice were anaesthetized by ketamine/xylazine injection i.p. and injected i.c.v. (into the cisterna magna) with 5 µl of QDot655 (Invitrogen) or 5 µl of Alexa488-conjugated anti-Lyve-1 antibody (ALY7, eBioscience). Mice were co-injected i.v. with 25 µl of 10% fluorescein sodium salt (Sigma-Aldrich) or 5 µl of QDot655 (Invitrogen). Meningeal lymphatic vessels were imaged through a thinned skull preparation. The core temperature of the mice was monitored and maintained at 37 °C. Imaging was performed with a Leica TCS SP8 multiphoton microscopy system (Leica Microsystems) equipped with a Chameleon Ultra II tunable Ti:Sapphire laser (Coherent). GFP and QDot655 were excited with an excitation wavelength of 880 nm. Images were obtained using a ×25 water immersion objective with 0.95 NA and external HyD non-descanned detectors (Leica Microsystems). Four-dimensional imaging data were collected by obtaining images from the x, y, and z-planes over time. The resulting images were analysed with Imaris software (Bitplane).

Labelling of the vascular compartment. To assess the abluminal localization of the sinusal T cells, mice were injected i.v. with 10 µg of FITC-conjugated anti-CD45 antibody (eBioscience, clone 30-F11) or control isotype 1 h before euthanasia. To assess that the meningeal lymphatic vessels are not part of the cardiovascular, mice were injected with 100 µl of DyLight 488 Lycopersicon Esculentum Lectin (Vector Laboratories) 5 min before euthanasia.

In vivo VEGFR3 activation. Mice were injected i.c.v. with 4 µg of rh-VEGF-c (Cys156Ser, R&D Systems) or with PBS. Meninges were harvested 7 and 14 days after the injection.

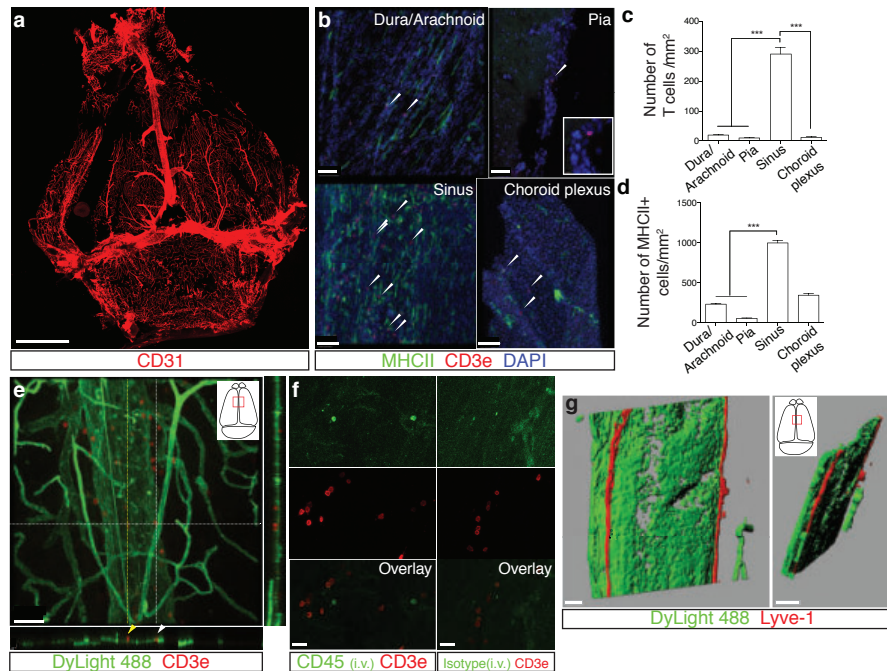
Evans blue injection and detection. Mice were anaesthetized by ketamine/xylazine injection i.p., and then 5 µl of 10% Evans blue (Sigma-Aldrich) was injected i.c.v. into the cisterna magna or intranasally. Thirty minutes after injection, mice were euthanized with CO₂ and the central nervous system draining lymph nodes were dissected for assessment of Evans blue content. The dura mater was also harvested to analyse Evans Blue localization using confocal microscopy. The intensity of the Evans blue was measured using the plot profile function of FIJI.

Flow cytometric analysis of meninges. Mice were perfused with 0.1 M PBS for 5 min. Heads were removed and skulls were quickly stripped. Mandibles were removed, as well as all skull material rostral to maxillae. Surgical scissors were used to remove the top of the skull, cutting clockwise, beginning and ending inferior to the right post-tympanic hook. Meninges (dura mater, arachnoid and pia mater) were carefully removed from the interior aspect of the skulls and surfaces of the brain with Dumont #5 forceps (Fine Science Tools). Meninges were gently pressed through 70 µm nylon mesh cell strainers with sterile plastic plunger (BD Biosciences) to yield a single-cell suspension. For lymphatic endothelial cells isolation, meninges (along with diaphragm and ear skin) were digested for 1 h in 0.41 U ml⁻¹ of Liberase TM (Roche) and 60 U ml⁻¹ of DNase I. Cells were then centrifuged at 280g at 4 °C for 10 min, the supernatant was removed and cells were resuspended in ice-cold FACS buffer (pH 7.4; 0.1 M PBS; 1 mM EDTA; 1% BSA). Cells were stained for extracellular marker with antibodies to CD45-PacificBlue

(BD Bioscience), CD45-phycoerythrin (PE)-Cy7 or eFluor 450 (eBioscience), TCR β -Alexa780 (eBioscience), CD4-Alexa488 (eBioscience), CD8-peridinin chlorophyll (PerCP)-Cy5.5 (eBioscience), CD44-allophycocyanin (APC) (eBioscience), CD62L-PE (eBioscience), CD71-APC (eBioscience), podoplanin-PE (eBioscience), CD31-Alexa647 (eBioscience), B220-PE (eBioscience), CD19-BB515 (BD Bioscience). Except for the lymphatic endothelial cells identification experiment, all cells were fixed in 1% PFA in 0.1 M pH 7.4 PBS. Fluorescence data were collected with a CyAn ADP High-Performance Flow Cytometer (Dako) or a Gallios (Beckman Coulter) then analysed using FlowJo software (Treestar). To obtain accurate cells counts, single cells were gated using the height, area and the pulse width of the forward and side scatter, then cells were selected for being live cells using the LIVE/DEAD Fixable Dead Cell Stain Kit per the manufacturer's instructions (Invitrogen). The cells were then gated for the appropriate markers for cell type (Extended Data Figs 3, 9). Experiments were performed on meninges

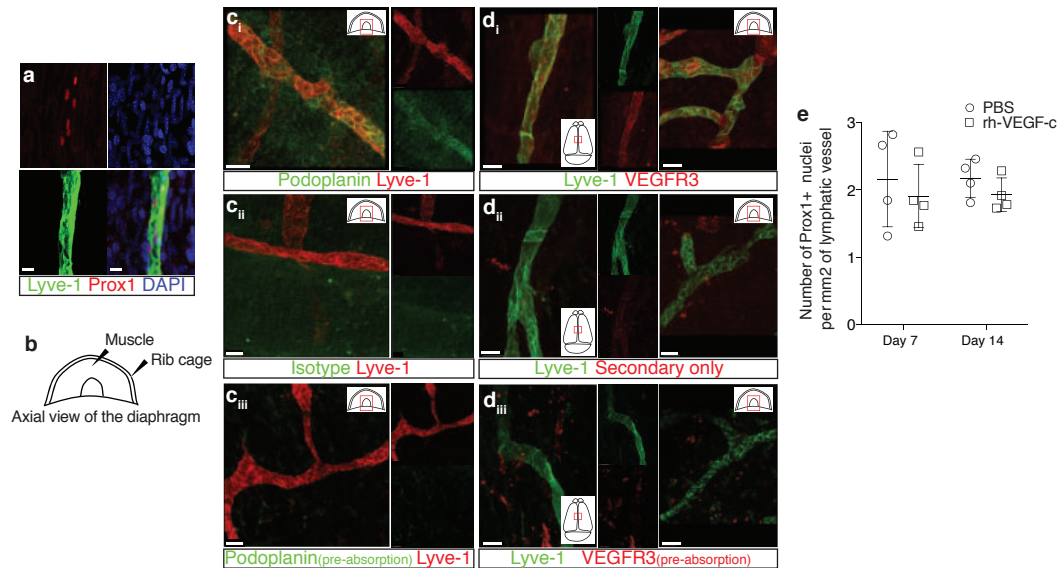
from $n = 3$ mice per group. Data processing was done with Excel and statistical analysis was performed using GraphPad Prism.

Deep cervical lymph node resection, ligation and sham surgery. Eight-week old mice were anaesthetized with ketamine/xylazine, shaved at the neck and cleaned with iodine and 70% ethanol, and an ophthalmic solution was put on the eyes to prevent drying. An incision was made midline 5 mm superior to the clavicle. The sternocleidomastoid muscle (SCM) was retracted, and the deep cervical lymph node was removed with forceps. For the ligation experiment, the collecting lymphatic vessels anterior to the deep cervical lymph nodes were ligated using a nylon suture (9-0 Ethilon black 6"VAS100-4). Sham-operated mice received the incision and had the SCM retracted, but were not ligated or the lymph nodes were not removed. Mice were then sutured and allowed to recover on a heating pad until responsive. Post-surgery, mice were given analgesic in the drinking water: 50 mg l⁻¹ for 3 days post-surgery and 0.16 mg for the next 2 weeks.



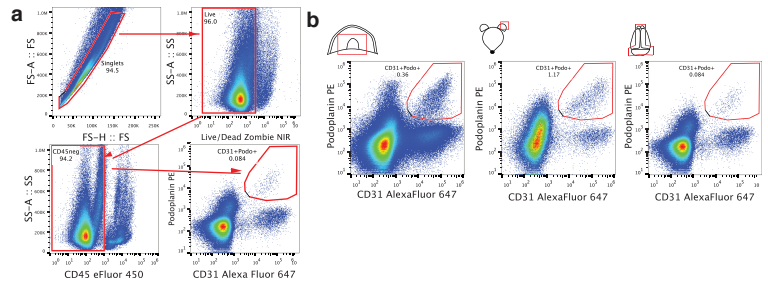
Extended Data Figure 1 | Meningeal immunity and lymphatic vessels in the dural sinuses. **a**, Representative image of CD31 staining in whole-mount meninges (scale bar, 2,000 μm). **b**, Representative images of T cells (CD3e, arrowheads) in the dura/arachnoid, pia, dural sinuses, and choroid plexus (scale bars, 70 μm). **c**, Quantification of T-cell density in different meningeal compartments (mean \pm s.e.m.; $n = 6$ animals each group from 2 independent experiments; $***P < 0.001$; Kruskal–Wallis test with Dunn’s post hoc test). **d**, Quantification of MHCII-expressing cells in different meningeal compartments (mean \pm s.e.m.; $n = 6$ animals each group from 2 independent experiments; $***P < 0.001$; Kruskal–Wallis test with Dunn’s post hoc test). **e**, Adult mice were injected i.v. with 100 μl of DyLight 488 lectin 5 min before euthanasia to enable labelling of the cardiovascular system. Meninges were harvested and stained with anti-CD3e. Representative orthogonal images of T-cell localization in the lumen (white arrowhead) and outside of the sinus (yellow arrowhead; $n = 2$ mice; scale bar, 70 μm). **f**, Adult mice were injected

i.v. with 10 μg of FITC-conjugated anti-CD45 antibody or FITC-conjugated isotype antibody. Meninges were harvested one hour after the injection and labelled with anti-CD3e. Representative images of CD3e immunolabelling around dural sinuses are shown. CD45-positive cells do not co-localize with CD3e⁺ cells (**a**), suggesting an abluminal localization of the latter ($n = 2$ mice each group; scale bars, 20 μm). **g**, Representative 3D reconstruction of the lymphatic vessels localization around the superior sagittal sinus. Adult mice were injected i.v. with 100 μl of DyLight 488 lectin 5 min before euthanasia in order to stain the cardiovascular system. Meninges were harvested and labelled with anti-Lyve-1. The lack of lectin staining in the Lyve-1-positive meningeal lymphatic vessels suggests that they are independent of the cardiovascular system ($n = 3$ mice; scale bars, left, 50 μm and right, 120 μm). The mounting of the whole meninges results in the flattening of the sinus, thus it does not appear tubular.



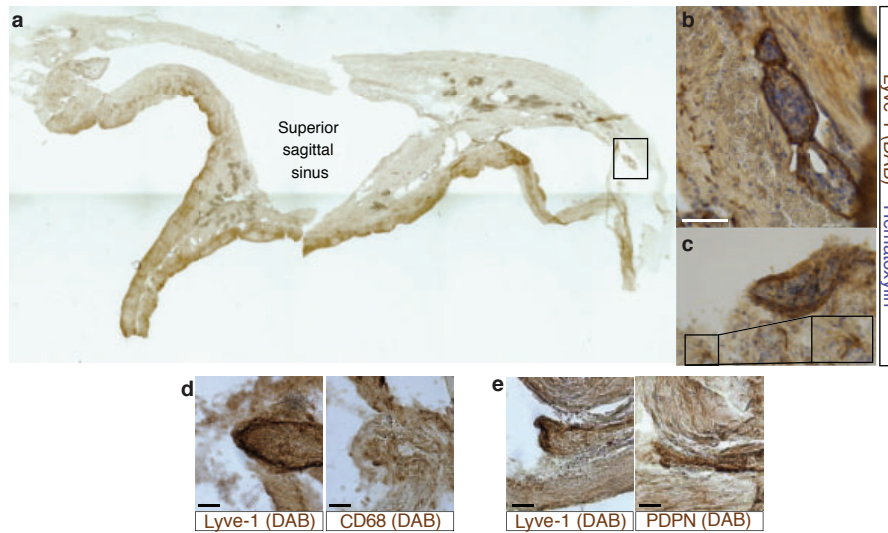
Extended Data Figure 2 | Identification, characterization and validation of the expression of classical lymphatic endothelial cell markers by the meningeal lymphatic vessels. **a**, Representative images of Prox1 labelling on meningeal Lyve-1 expressing vessels ($n = 3$ mice; scale bars, $10 \mu\text{m}$). **b**, Schematic representation of the whole-mount dissection of the diaphragm. **c**, Characterization of the specificity of the podoplanin antibody. Representative images of whole-mount diaphragm labelled with anti-Lyve-1 and anti-podoplanin (**c_i**), control isotype (**c_{ii}**) or the anti-podoplanin pre-

incubated overnight with a saturated concentration of recombinant podoplanin protein (**c_{iii}**; scale bars, $20 \mu\text{m}$). **d**, Characterization of the specificity of the VEGFR3 antibody. Representative images of whole-mount diaphragm and dura mater labelled with anti-Lyve-1 and anti-VEGFR3 (**d_i**), secondary antibody only (**d_{ii}**), or the anti-VEGFR3 pre-incubated overnight with a saturated concentration of recombinant VEGFR3 protein (**d_{iii}**; scale bars, $20 \mu\text{m}$). **e**, Quantification of the number of Prox1⁺ nuclei per mm² of lymphatic vessel (mean \pm s.e.m.; $n = 4$ animals each group).



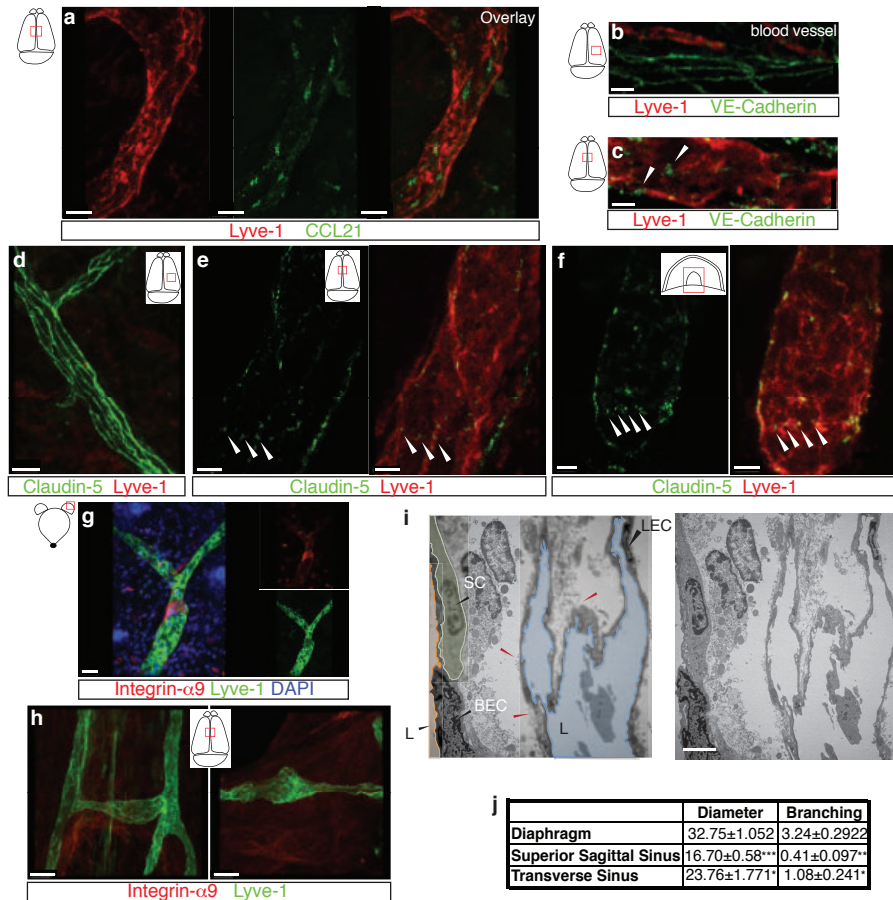
Extended Data Figure 3 | Identification of the meningeal lymphatic endothelial cell population by flow cytometry. FACS analysis of the lymphatic endothelial cells in diaphragm, skin (ear), and dural sinuses. **a**, Gating strategy employed to identify lymphatic endothelial cells (CD31⁺podoplanin⁺).

Lymphatic endothelial cells are identified as singlet, live cells, CD45⁻ and CD31⁺podoplanin⁺. **b**, Representative dot plots for lymphatic endothelial cells (CD31⁺podoplanin⁺) in the diaphragm, skin, and dura mater of adult mice.



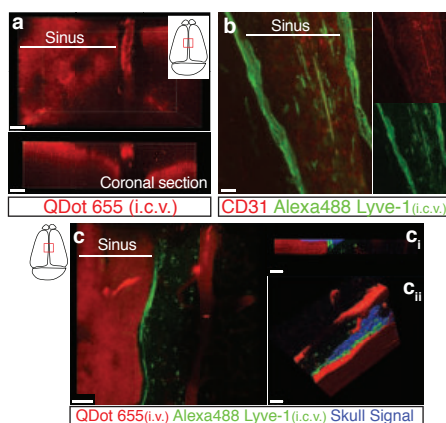
Extended Data Figure 4 | Pilot identification of lymphatic vessels in human dura. **a**, Representative image of a formalin-fixed coronal section of human superior sagittal sinus. **b**, **c**, Representative images of Lyve-1 staining on coronal section of human superior sagittal sinus (scale bar, 100 μ m). The box in **c** highlights the presence of Lyve-1-expressing macrophages in human

meninges, as seen in mice. **d**, Representative images of Lyve-1 and CD68 staining of coronal sections of human superior sagittal sinus. Note the absence of CD68 positivity on Lyve-1 positive structures (scale bars, 50 μ m). **e**, Representative images of podoplanin and Lyve-1 staining of coronal sections of human superior sagittal sinus (scale bars, 50 μ m).



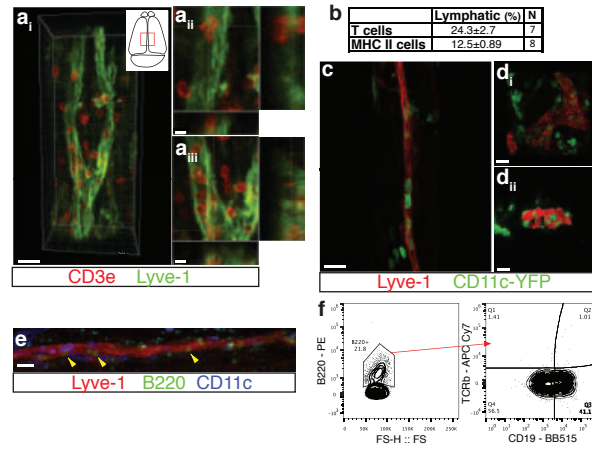
Extended Data Figure 5 | Initial lymphatic features of meningeal lymphatic vessels. **a**, Representative images of CCL21 and Lyve-1 labelling of the meningeal lymphatic vessels (scale bars, 10 μ m). **b, c**, Representative images of VE-Cadherin and Lyve-1 staining on meningeal blood vessels (**b**) and meningeal lymphatic vessels (**c**), arrowheads point to the VE-Cadherin aggregates; scale bars, 10 μ m). **d-f**, Representative images of Claudin-5 and Lyve-1 staining on meningeal blood (**d**) and lymphatic (**e**) vessels, and diaphragm lymphatic vessels (**f**); arrowheads point to Claudin-5 aggregates (scale bars, 10 μ m). **g, h**, Representative images of integrin- α 9 and Lyve-1 labelling on skin (**g**; ear) and meninges whole mount (**h**). Scale bars, 40 μ m. No integrin- α 9 expressing valves were detected in the meningeal lymphatic vessels.

i, Representative low power micrographs (transmission electron microscopy) of the meningeal lymphatic vessels (scale bar, 2 μ m); L, lumen; SC, supporting cell; LEC, lymphatic endothelial cell; BEC, sinusal endothelial cell. Red arrowheads point to anchoring filaments. **j**, Table summarizing morphological features of the lymphatic network in different regions of the meninges and the diaphragm. Diameters are expressed in μ m and branching as number of branches per mm of vessel; (mean \pm s.e.m.; $n = 4$ animals each group from 2 independent experiments, * $P < 0.05$, ** $P < 0.01$, *** $P < 0.001$; two-way ANOVA with Bonferroni post hoc test). For statistics, the presented comparisons were between the diaphragm and the superior sagittal sinus and between the superior sagittal sinus and the transverse sinuses.



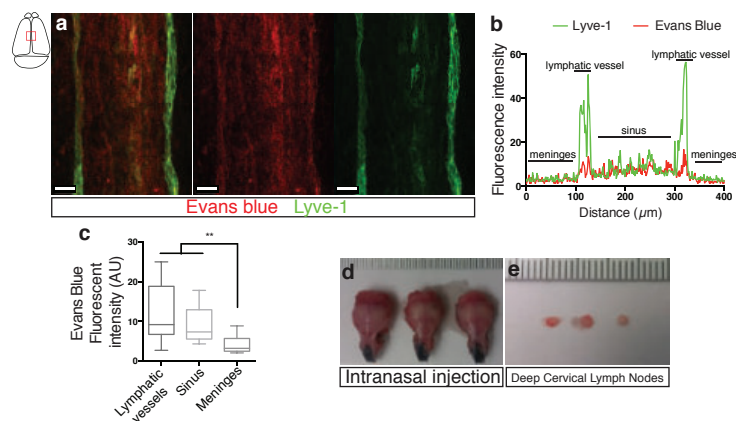
Extended Data Figure 6 | Drainage of cerebrospinal fluid into the meningeal lymphatic vessels. **a**, Representative z-stack of QDot655 filled cerebrospinal fluid drainage both in the blood vasculature (sinus) and in the meningeal lymphatic vessels after i.c.v. injection (scale bar, 20 μm). **b**, Representative images of CD31 and Lyve-1 immunostaining on whole-mount meninges. Adult mice were injected i.c.v. with 2.5 μg of Alexa488 conjugated anti-Lyve-1 antibody. Thirty minutes after the injection, the meninges were harvested and stained with anti-CD31. Injected *in vivo*, the

Lyve-1 antibody illuminates the lymphatic vessels (scale bar, 20 μm). **c**, Representative z-stack of the superior sagittal sinus of adult mice injected i.v. with QDot655 and i.c.v. with Alexa488 conjugated anti-Lyve-1 antibody. **c_i**, Coronal section of the z-stack presented in panel c. The signal from the remaining skull and/or collagen-rich structure above the meninges was recorded (blue). **c_{ii}**, 3D reconstruction of the z-stack presented in panel c showing the localization of the meningeal lymphatic vessels under the skull (scale bars, 50 μm).



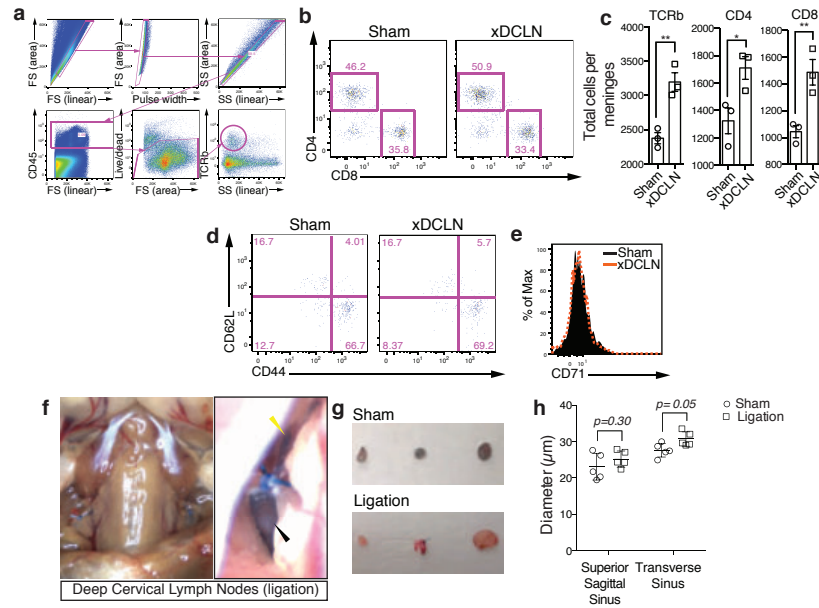
Extended Data Figure 7 | Meningeal lymphatic vessels carrying immune cells. **a**, Representative images of T cells (CD3e) and lymphatic endothelial cells (Lyve-1) on dural sinuses (scale bar, 20 μ m). **a_{ii}**–**a_{iii}**, Orthogonal sections representing T-cell localization around **a_{ii}** and within **a_{iii}** the Lyve-1 structures (scale bars, 5 μ m). **b**, Quantification of the sinusal T cells and MHCII-expressing cells within the lymphatic vessels (mean \pm s.e.m., $n = 7$ –8 mice from 3 independent experiments). **c**, **d**, Representative images of Lyve-1

staining on dural meninges from CD11c^{YFP} mice (scale bars, 20 μ m). CD11c-positive cells (most probably dendritic cells) can be found inside the meningeal lymphatic vessels. **e**, Representative image of B220⁺ cells and lymphatic endothelial cells (Lyve-1) immunolabelling in the meninges (yellow arrowheads indicate B220⁺CD11c⁻ cells; scale bar, 20 μ m). **f**, Representative dot plots of B220⁺ cells (gated on singlets, live, CD45⁺) within the dural sinuses expressing CD19; ~40% of the B220⁺ cells express CD19.



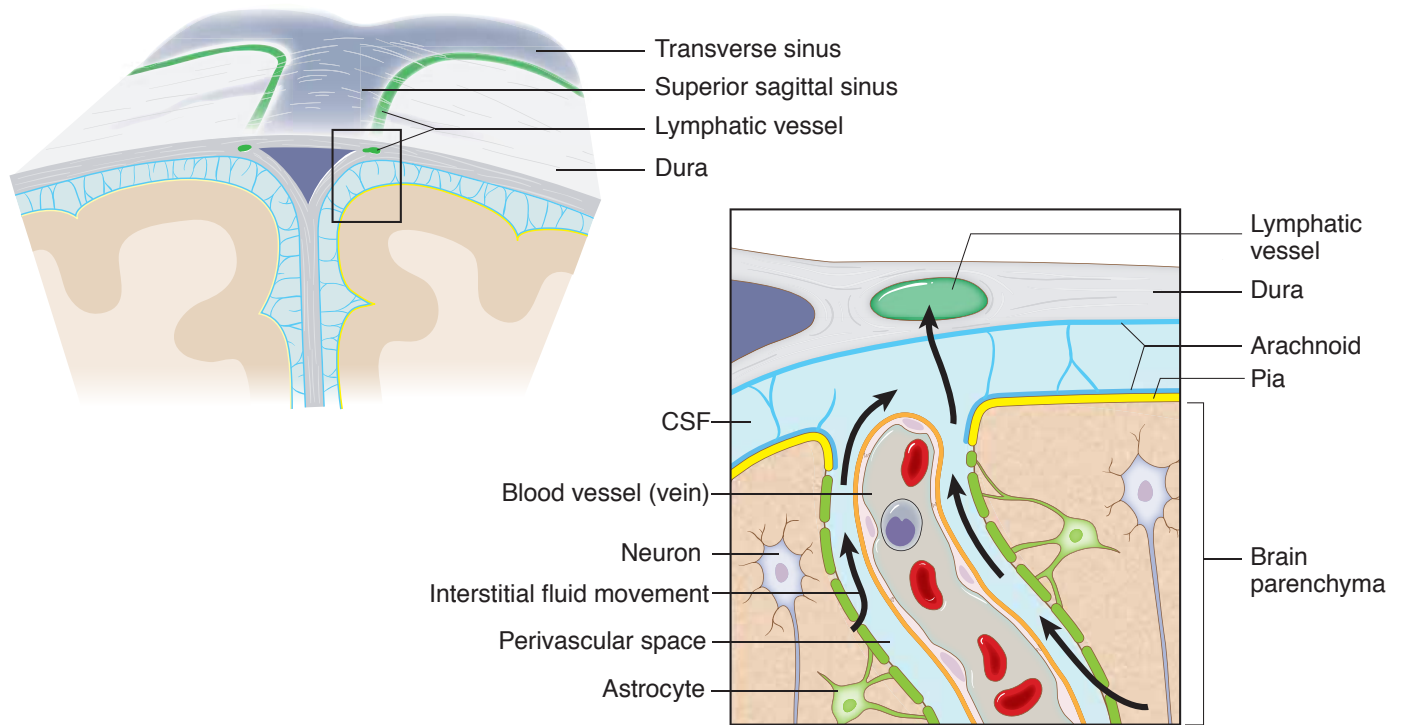
Extended Data Figure 8 | Drainage of Evans blue from the meningeal lymphatic vessels but not the nasal mucosa into the deep cervical lymph nodes. **a–c**, Adult mice were injected i.c.v. with 5 μl of 10% Evans blue. The meninges were harvested 30 min after injection and Evans blue localization was assessed by confocal microscopy. **a**, Representative images of Evans blue localization in both the sinus and the meningeal lymphatic vessels ($n = 9$ mice; scale bars, 40 μm). **b**, Representative profile of Evans blue and Lyve-1 relative fluorescence intensity on a cross-section of the image presented in **a**.

c, Quantification of the average intensity of Evans blue in the sinus, the lymphatic vessels and the meninges of adult mice (mean \pm s.e.m., $n = 16$ analysed fields from 4 independent animals; $**P < 0.01$, Kruskal–Wallis with Dunn’s multiple comparisons test). **d**, **e**, Adult mice were injected intranasally with 5 μl of 10% Evans blue. The successful targeting of the nasal mucosa (**d**) and the lack of accumulation of Evans blue in the deep cervical lymph nodes (**e**) 30 min after the injection are demonstrated.



Extended Data Figure 9 | Effects of deep cervical lymph node resection and of the lymphatic vessels ligation on the meningeal immune compartment. **a–e**, The deep cervical lymph nodes were resected (xDCLN) or sham-operated. Three weeks after resection, the meninges were harvested, single cells isolated, and analysed for T-cell content by flow cytometry. **a**, Gating strategy to analyse meningeal T cells. Meningeal T cells are selected for singlets, CD45⁺, live cells and TCRβ⁺. **b**, Representative dot plot for CD8⁺ and CD4⁺ T cells in meninges of sham and xDCLN mice. **c**, Quantification of total T cells (TCRβ⁺), CD4⁺ and CD8⁺ in the meninges of xDCLN and sham mice (mean ± s.e.m.; $n = 3$ animals each group; * $P = 0.018$; ** $P = 0.006$ (CD8), $P = 0.003$ (TCRb); Student's t -test; a representative experiment, out of two independently performed, is presented). **d**, Representative expression of CD62L and CD44 by CD4⁺ T cells phenotype in sham and xDCLN mice ($n = 3$ mice per group). **e**, Representative histogram for CD71 expression by meningeal CD4⁺ T cells in

sham and xDCLN mice ($n = 3$ mice per group). **f**, Representative images of the ligation surgery. To highlight the lymph vessels, Evans blue was injected i.c.v. before the surgery. Black arrowhead points to the node, yellow arrowhead points to the ligated Evans blue-filled vessels. **g**, Sham-operated or ligated animals were injected i.c.v. with 5 µl of 10% Evans blue. The deep cervical lymph nodes were harvested 30 min after the injection and analysed for Evans blue content. Representative images of the Evans blue accumulation in the deep cervical lymph nodes of the sham-operated and ligated animals are presented. **h**, Quantification of the meningeal lymphatic vessel diameter in the superior sagittal sinus and the transverse sinuses in sham mice and after ligation of the collecting lymphatic vessels (mean ± s.e.m., $n = 5$ mice per group from 2 independent experiments; two-way ANOVA with Bonferroni post hoc test).



Extended Data Figure 10 | Connection between the glymphatic system and the meningeal lymphatic system. A schematic representation of a connection between the glymphatic system, responsible for collecting of the interstitial

fluids from within the central nervous system parenchyma to cerebrospinal fluid, and our newly identified meningeal lymphatic vessels.